Design and performance assessment of modular multi-band photonic-integrated WSS

Design and Performance Assessment of Modular Multi-band Photonic-integrated WSS

LORENZO TUNESI,[1,*] IHTESHAM KHAN,[1] MUHAMMAD UMAR MASOOD,[1] ENRICO GHILLINO,[2] VITTORIO CURRI,[1] ANDREA CARENA,[1] PAOLO BARDELLA[1]

[1]*Politecnico di Torino, Corso Duca degli Abruzzi, 24, 10129, Torino, Italy*
[2]*Synopsys, Inc., 400 Executive Blvd Ste 101, Ossining, NY 10562, United States*
[*]*lorenzo.tunesi@polito.it*

Abstract: Today, optical transport and data center networks extensively utilize photonic integrated systems due to their large bandwidth and a high degree of reconfigurability. In addition to these properties, photonic integrated-based systems can deliver an overall low fabrication cost, a small footprint, and low power consumption. In this perspective, we present a modular photonic integrated multi-band Wavelength Selective Switch (WSS) capable of managing a wide spectrum, covering the three S+C+L bands, and potentially scalable to larger numbers of output fibers and routed channels. We propose a complete description of the device starting from the physical level, commenting on the device's internal structure and design-related issues. Then, we move to the transmission level, providing a complete abstraction of the proposed WSS in the context of software-defined optical networks by providing a deterministic model to evaluate the routing controls, thermal spectral tunability, and the quality of transmission degradation. Finally, a transmission scenario operating on 400ZR standards and a network case study are also demonstrated to evaluate the performance of the proposed WSS in a single or multistage cascade setup.

1. Introduction

The traffic analysis of telecommunication networks shows an annual increase in bandwidth between 20% and 60% during the last decade [1]. This growth trend will be further enhanced due to the commercialization of 5G and the increasing application of the Internet of Things (IoT) framework. Forecasts indicate that this rapid increase will soon push state-of-the-art transparent optical networks towards saturation as we enter the Zettabyte era [2]. To accommodate this, service providers must increase capacity by implementing cost-effective, scalable, and flexible solutions. In this interest, they always aim to take advantage of the residual capacity of the already deployed network infrastructure to maximize CAPEX returns.

Today, state-of-the-art optical transport is mainly operated by transparent propagation of Wavelength Division Multiplexing (WDM) channels that exploit dual-polarization coherent optical technologies over the entire C-band, in a spectral window of 4.8 THz with a maximum transmission capacity of about 10 Tbps per fiber [3]. Additional capacity can be achieved by adopting modern transceivers (TRXs) that can flexibly adapt the transmission rate corresponding to the available Quality-of-Transmission (QoT) on the given transparent optical path. In the same way, WDM optical transport can be enhanced from a fixed grid to a flex grid to optimize spectral usage. Unfortunately, the margin for capacity increase based on these approaches is quite limited as they already operate close to their theoretical limits.

Multi-Band Transmission (MBT) is a potential solution to add additional capacity to an already deployed network infrastructure, targeting the transmission of WDM channels over the entire low-loss optical spectrum. Most of the state-of-the-art optical networks are based on standard step-index single-mode fibers without water absorption peak (ITU-T G.652D fibers) where the

low-loss region extends from the O- to the L-band (1260 nm to 1625 nm) delivering a potentially available spectrum exceeding 50 THz [4]. Along with this, different amplifier prototypes are now functional to operate on new spectral bandwidths [5]. Therefore, exploiting additional spectrum for MBT is generally the most economical solution to enhance capacity, as it does not need capital expenditure to deploy new fiber infrastructure.

Apart from multi-band amplifiers, the deployment of MBT also requires the availability of filtering and switching modules to enable transparent wavelength routing. A key element in WDM switching architecture is the Wavelength Selective Switch (WSS), which enables independent control and routing of each input WDM channel toward one of the fiber outputs. Traditionally, WSSs are implemented through Micro-Electro-Mechanical Mirrors (MEMS) and Liquid Crystal on Silicon (LCoS), resulting in devices that are usually bulky, expensive, and complex in manufacturing, implementation, and maintenance [6]. In contrast, WSS implementation using the fast emerging technology of Photonic Integrated Circuits (PICs) can offer a cost-effective solution with a small footprint and massive production capabilities [7].

Effective wavelength switching is a main element for implementing the software-defined network (SDN) down to the physical layer, since it enables dynamic and efficient management of the massive bandwidth in the MBT framework. Applications of the SDN paradigm down to the WDM optical transport layer enable the complete virtualization of WDM optical transport using a standard Application Programming Interface (API). In this application, both network elements and transmission functionalities must be abstracted to allow evaluation of QoT impairments and control prediction. This approach enables the autonomous management of each network element using standard APIs in the control plane [8–10]. In this context, proper modeling is required for the control and the evaluation of QoT impairment, as it has a significant role in accurately estimating the Optical Signal-to-Noise Ratio (OSNR) of transparent lightpaths (LPs). This is an enabler in achieving the maximization of deployed capacity.

In this work, we take advantage of the integration allowed by silicon photonics technology by proposing a novel integrated device working as a multi-band WSS. It supports WDM MBT using a modular architecture and can be operated in a wide range of the optical spectrum, covering the S+C+L bands. To this end we aim to provide a comprehensive vertical study, ranging from the design strategy at the device level, up to the extraction and characterization of the transmission level penalties and impairments. The architectural design of the novel modular WSS, described in Section II, is easily scalable to account for more output fibers and a larger number of channels with a smaller footprint than traditional MEMS-based implementations. Furthermore, in addition to the analysis of the design step, in Section III, we perform a complete characterization and abstraction of the proposed WSS in the context of the SDN paradigm. The APIs running on the SDN controller are utilized for control and take advantage of the QoT degradation model to implement the SDN applications down to WDM transport. The proposed control and QoT penalty evaluation model enable complete control of the proposed multi-band modular WSS by a centralized network controller. Finally, Section IV presents a case study of the WSS device in a realistic networking scenario, followed by a conclusion in Section V.

2. Design of the Wavelength Selective Switch

The proposed device is a PIC that enables wavelength switching in a multi-band scenario. It has been designed to operate in the S+C+L optical telecommunication bands, allowing independent routing of every channel of the input WDM comb to a target output fiber. In the proposed implementation scenario, the module has been designed with three target output fibers, allowing the switching operation for M=8 channels centered in each of the considered bands, with a total of 24 independently controlled channels. The filtering elements are optimized for the target frequencies in the S+C+L bands, with a channel separation of 100 GHz. The underlying structure is modular and expandable, allowing for scalability of the proposed implementation for a higher

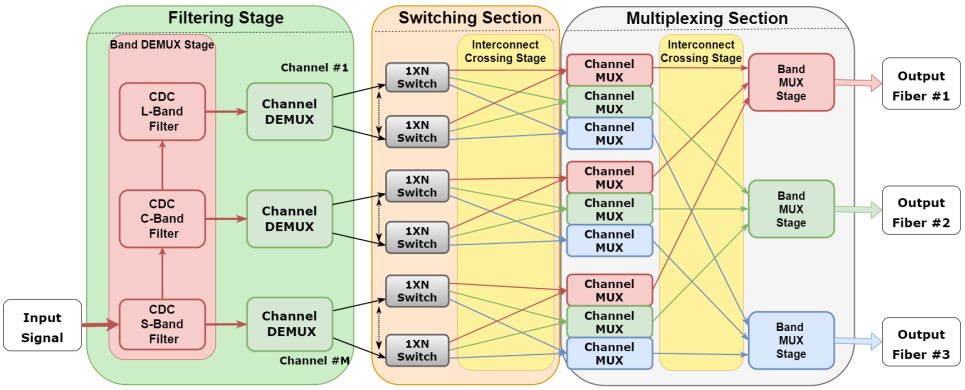

Fig. 1. General structure of the proposed 1×3 WSS.

number of channels and/or target output fibers.

The model of the proposed circuit is depicted in Fig. 1, which highlights the general structure with the different stages allowing the WSS operation. The device can be divided into three main sections, handling the demultiplexing, switching, and multiplexing operation. The first section is tasked with separating each individual channel of the WDM comb, minimizing loss and channel interference, while the second section is responsible for routing each of the separate channels to the required output fiber. The third section, tasked with multiplexing the signals onto the output fibers, mirrors the first section, recreating the WDM combs and multiplexing each band onto a common waveguide. Each stage is described in the following sections. We describe all physical components and the design strategies we followed in the proposed implementation. Moreover, we also discuss the general expansion of the device. The internal structure of the stages can be seen in Fig. 2, which depicts the generalized structure of the channel filtering cascade, as well as the arbitrary sized 1×N switching network topology. In the case analyzed, the filtering cascade is designed for the 8 target channels in each band, while the switching network is a simpler 1×3 structure; as depicted, the multiplexing structure mirrors the demux stage, using the same number

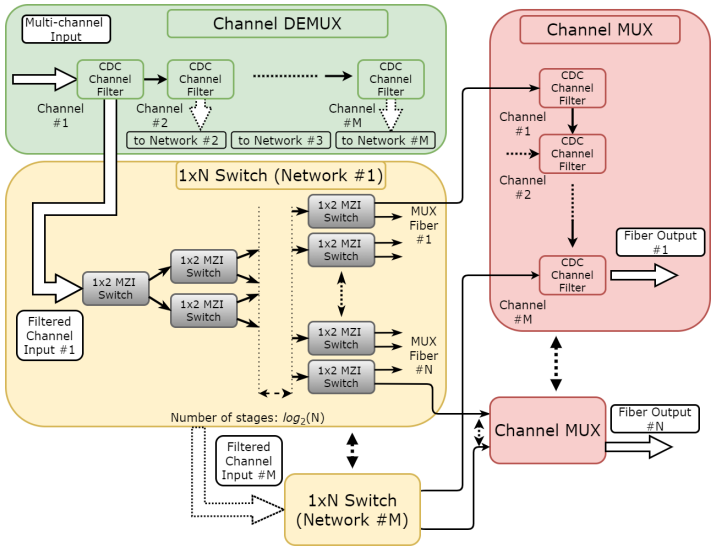

Fig. 2. Filtering stages cascade and switching architecture.

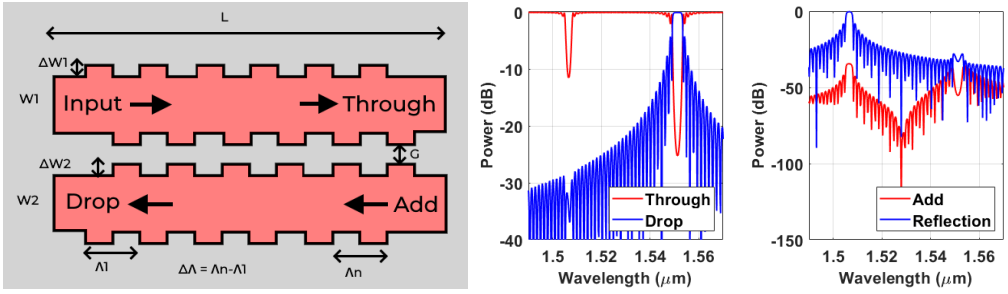

(a) Generic Structure for a Contra-Directional Coupler. (b) Response at each port for a typical CDC add-drop.

Fig. 3. Contra-DC coupler filter.

of add-drop elements for each target output fiber.

With respect to the waveguide geometry used in the simulations, we assume Silicon Photonics waveguides with width $W = 0.55\,\mu m$ and height $H = 0.22\,\mu m$: ideal tapered structures are assumed when changes in the waveguide widths are required.

2.1. Filtering section

The main objective of the filtering section, as described before, is to separate each individual channel, while keeping losses and crosstalk to a minimum. Our approach to this problem is based on multiple stages of filtering. The first stage is tasked with separating the S+C+L bands to avoid inter-band interference, while the second stage selects individually each channel; at the same time, splitting the filtering structure into multiple parallel sections helps reduce the losses, reducing the overall length of the add/drop filters cascade.

The fundamental component that is used for this device implementation is the Grating-Assisted Contra-Directional Coupler (GACDC) add-drop filter, more simply referred to as Contra-Directional Coupler (CDC). CDCs are extremely flexible integrated devices that can be designed to cover a wide range of add-drop applications, ranging from high Extinction Ratio (ER) narrow filters to ultra-wideband applications. These four-port devices are based on wavelength-selective coupling between the forward mode of one waveguide and the backward-propagating mode of the second one: by proper design of the periodic index perturbations in the waveguides, the overall add-drop response can be precisely tailored to the required scenario. In our analysis, we model the devices based on well-known Coupled-Mode Theory (CMT) models [11], which have a high degree of accuracy with respect to the experimental devices.

The general structure and response of a CDC add/drop is depicted in Fig. 3: while the devices are characterized by their waveguides and gratings geometries, their behavior can be simulated based on simplified coefficients and variables, such as coupling (κ_{11}, κ_{12}, κ_{22}), length (L), grating pitch (Λ), and waveguide effective indices. The gap between the two waveguides G, is modeled through the contra-directional coupling κ_{12}, which have been designed to achieve the target response while accounting for experimental-backed results available in the literature, as described in the following design optimizations steps.

As shown in the figure, in their straightforward implementation they exhibit a non-ideal ER as well as a high backward reflection peak, which is incompatible with the desired DWDM target implementation: to improve the response of the filters, more advanced design strategies have been considered, which will be discussed for both the band filtering and channel filtering elements.

As previously stated, the first stage of the demultiplexer is tasked with separating the bands of operation, allowing the reduction of the losses and limiting inter-band interference. This operation requires a flat-top wide-band response, which can be achieved through a precise variation of the perturbation period along the device [12], also known as pitch chirping ($\Delta\Lambda$): by gradually

	S-band	C-band	L-band
Λ (nm)	275	293	302
$\Delta\Lambda$ (nm)	20	9	18
L (mm)	1.5	0.8	1.4
$W1$ (nm)	570		
$\Delta W1$ (nm)	100		
$W2$ (nm)	430		
$\Delta W2$ (nm)	60		

$\kappa_{11} = \kappa_{22}$ (cm^{-1})	10
$\kappa_{12,\max}$ (cm^{-1})	115
$\kappa_{12}(z)$ (cm^{-1})	Hyperbolic tangent apodization $\frac{\kappa_{12,\max}}{2}\left[1+\tanh\left(b\left(1-2\left\lvert\frac{z}{L}-\frac{1}{2}\right\rvert^{a}\right)\right)\right]$ $a=3, b=2$
Loss α (dB cm^{-1})	1.8

Table 1. Band Contra-DC filters design parameters.

	S-band	C-band	L-band
Λ_1 (nm)	284.2	298.9	312.6
Λ_2 (nm)	284.0	298.7	312.4
Λ_3 (nm)	283.8	298.5	312.1
Λ_4 (nm)	283.6	298.2	311.9
Λ_5 (nm)	283.4	298.0	311.6
Λ_6 (nm)	283.2	297.8	311.4
Λ_7 (nm)	283.0	297.6	311.0
Λ_8 (nm)	282.8	297.3	310.9

L (mm)	0.940
$\kappa_{11} = \kappa_{22}$ (cm^{-1})	10
$\kappa_{12,\max}$ (cm^{-1})	35
$\kappa_{12}(z)$ (cm^{-1})	Gaussian apodization $\kappa_{12,\max}\exp\left(-a\left(\frac{z}{L}-\frac{1}{2}\right)^{2}\right)$ $a=6$
Loss α (dB cm^{-1})	1.8

Table 2. Channel filters parameters and main model parameters

increasing the pitch (Λ) the band can be extended while maintaining the same flatness and limited insertion losses. The response of the three main filters is depicted in Fig. 4a, while the simulation parameters are reported in Table 1. Furthermore, to improve the Side-Lobe Suppression Ratio (SLSR) the grating profile is apodized, smoothing the transition between the standard unperturbed waveguide and the high-coupling region. By avoiding abrupt coupling changes along the device, the side lobes are reduced, limiting cross-talk and interference: two of the most used apodization profiles are the gaussian and the hyperbolic tangent; while the gaussian profile can achieve larger side-lobe suppression, it also can affect the flatness of the pass band, especially in pitch-chirped

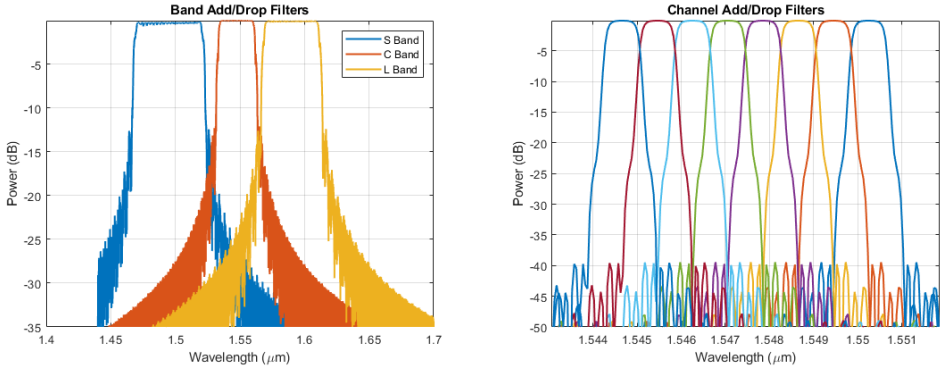

(a) Frequency Response for the Band filters.

(b) Frequency Response of the 8 channel stage (C-band).

Fig. 4. CDC filters response.

design. As such the trade-off is considered valid for the channel filter cases, while the band filter employ the hyperbolic tangent profile, which ensure the channel band and flatness. Finally, to suppress the backward reflection of the input waveguide, another technique is considered, which consists of using out-of-phase gratings that minimize the unwanted reflection peak [13].
After this initial band separation stage, the WDM combs are demultiplexed by parallel cascades of smaller CDCs, which are designed and simulated considering similar optimization strategies, although targeting a smaller bandwidth of operation. In the proposed case, considering channels with Free Spectral Range FSR= 100 GHz the resulting pitch Λ of each filtering element and their general simulation parameters are reported in Table 2, while their frequency response is depicted for the C-band subsection in Fig. 4b. From a design standpoint, channel filters differ from band filters due to the absence of pitch chirping, while also being optimized for a narrow drop band, which is typically difficult to achieve with CDCs structures [14]. The general design strategy for narrow-band implementations consist of trying to achieve low coupling coefficient and long coupling lengths, which can be further helped by the previously described gaussian apodization
Considering the same geometrical parameters for the waveguides, the frequency response for the elements can be obtained by considering weaker coupling structures, which can be designed for the target FRS: while the simulation model allows direct control over the κ parameters, in reality this can be achieved through a larger gap G or different corrugation geometry ΔW. As a reference, the required coupling values of κ_{12} for the channel and band filters can be obtained with waveguide gaps $G_{\text{ch}} = 300$ nm and $G_{\text{band}} = 200$ nm, respectively.

2.2. *Switching section and multiplexing*

After the filtering section, each individual channel is routed through a separate switching network, which allows targeting any of the output fibers. As already depicted in Fig. 2, this operation is achieved by cascading a series of 1×2 controllable Optical Switching Elements (OSE). The proposed switching network can be designed for any number of target output fiber N and is composed of $N-1$ OSE arranged in $\log_2(N)$ stages. The OSE implemented in these sub-networks consists of a Mach-Zehnder Interferometer (MZI) switch.

Unlike MRR-based OSE, MZI devices can easily achieve a large flat response, which makes them preferable in MBT applications because of their almost frequency-independent switching operation [15–17].

The MZI general structure is shown in Fig. 5a, which highlights the main physical design parameters together with the switching control section. By increasing the temperature of the highlighted arm of the MZI through a suitable electrical control signal, the device is driven between the two possible routing states (UP or DOWN). The electrical control and pads are

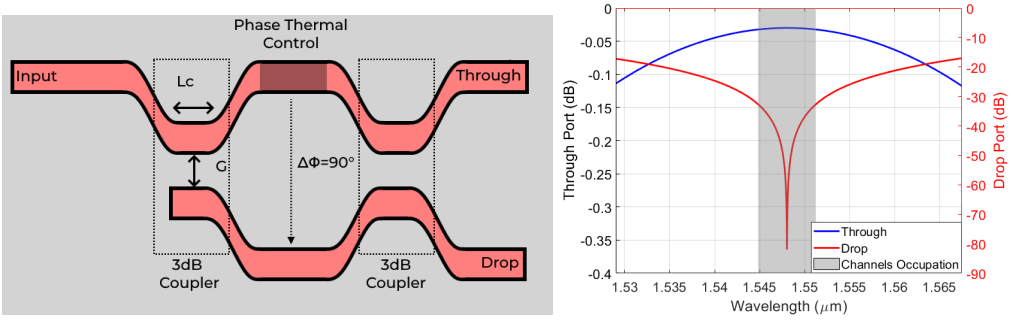

(a) (b)

Fig. 5. MZI-based tunable OSE for C-band applications. (a) MZI circuit schematic; (b) frequency response of the C-band implementation.

designed to meet the required switching performance and technological process [18]. As an example, considering the C-band, the frequency response for the off state (UP) is depicted in Fig. 5b, highlighting the region occupied by the target 8 channels: the device shows a remarkable flat response in the center of the design frequency, enabling the required frequency-independent switching operation. Similar performances are also achieved in the L- and S- bands.

The remaining stage of the device is the crossing and multiplexing stage: each of the outputs of the previous switching network must be properly connected and added to the egress waveguide of each output port. This dense interconnect region cannot be ignored as the transmission penalties are not negligible, while also introducing path-dependent degradation. Each individual waveguide crossing has been modeled to introduce 0.04 dB of insertion loss in the whole spectrum. State-of-the-art crossing technologies have been shown to yield even better performances [19–21], and therefore the flat value has been chosen to also account for the non-idealities of the actual implementation. As shown in Fig. 6 the proposed layout solution to reduce the number of crossings consists of a two-stage topology: by multiplexing the output of the switching network for each individual band, it is possible to confine the denser part of the crossing stage right after the switches, avoiding large-scale overlap of the output interconnects, while maintaining the same number of add/drop elements for the MUX operation.

It is evident how without any grouping strategy the overall complexity will increase. Taking into account the generic device with N output fibers and M channels per band, the highest number of crossings without any topology optimization is equal to $N_{\text{cross}} = (3M - 1)(N - 1)$. By grouping the connections into a middle stage, dividing the total number of channels into K arbitrary groups, the general trend can be reduced to $N_{\text{cross}} = (\frac{3M}{K} - 1)(N - 1) + (K - 1)(N - 1)$. The number of crossings is minimized when $K_{\text{opt}} = \lfloor \sqrt{3M} \rfloor$. This approach allows for a drastic reduction of the amount of crossing encountered by the propagating signal and results in the trend shown in the graph. It is important to note that this behavior represents the worst routing case, which applies only to a small number of routing instances with respect to the total number of routing states available, as will be shown in the later sections. Nevertheless, even considering the small effect of an individual waveguide crossing, it is clear how considerable differences in the resulting insertion and power loss may be expected between the nonoptimized and optimized cases, especially for large-scale implementations.

The current model does not include losses pertaining to the fiber-to-waveguide coupling at the ingress and egress stages of the device: the penalty model aims to characterize the operational elements of the internal architecture, such as filters and switches, as well as the path-dependent elements like the waveguide crossings. The effect of the different optical paths follows a similar assumption: while the waveguide crossings cannot be removed through topology changes while maintaining the architecture, the waveguide paths can be designed to minimize their effect on the channel comb, making them negligible with respect to the other passive elements.
The wavelength combiners tasked with multiplexing the signals onto the common waveguides have instead been modeled and simulated symmetrically with respect to the DEMUX region, described in detail in the previous section.

2.3. Insertion losses and layout

Before analyzing the path-dependant effects on the QoT and the transmission level penalties, the Insertion Losses (IL) and spectral characteristics of the device were evaluated.
This analysis is carried out considering a broadband flat input signal that covers the entire operating bandwidth (S+C+L), and measuring the output signal considering a single reference output port, as depicted in Fig. 7a. This representation takes into account the cascaded configuration of all filtering and switching elements, while the path-dependent effect of the crossing is not considered, as will be discussed and evaluated in detail in the QoT analysis. The reference IL of each component is reported in Fig. 7b. These values have been considered based on results

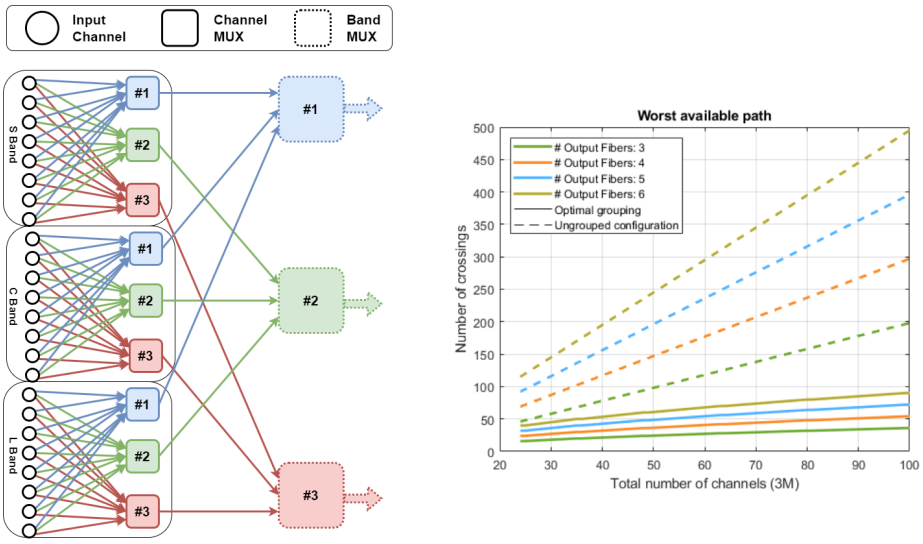

Fig. 6. Interconnect crossing stage topology with main MUX elements. $M = 8$, $N = 3$. On the right the comparison between non-optimized and optimized worst-path crossing cost is plotted.

available in the literature for the 1×2 MZIs used for switching [22] and the experimental literature of CDC used to optimize their design.

The insertion loss is almost flat between the channels due to the symmetric nature of the MUX/DEMUX blocks, which leads to each channel encountering the same number of CDCs elements: the first channel that is filtered out in the first stage is also the first to be multiplexed to the egress waveguide, as such propagation and cascading losses can be equalized between the channels. The three bands show a similar flat insertion loss, with a reference value of IL= 4.17 dB.

Overall this estimation of the insertion losses leads to compatible values with respect to other integrated solutions that take advantage of loopback AWG-based multiplexing and demultiplexing [23]. In this analysis, we have not considered the losses and path asymmetries due to the possible layout of an experimental implementation: It is assumed that the ideal placement of the device on the die can equalize this effect, making it negligible with respect to the effect of the main components. However, an estimate of the device footprint is provided in Table 3: for this evaluation, standard buffer spaces are considered around each component to avoid interference. The total footprint represents a reference value for the die space occupied by the sum of all components, although the waveguide bends and connecting segments would increase the actual size: despite this, the components footprint is shown to be manageable on standard-size chips.

	MZI	Band CDC	Channel CDC	Crossings
W (µm)	500	1500	900	20
H (µm)	6	6	6	20
# of elements	48	12	96	93
Footprint (mm^2)	0.144	0.108	0.5184	0.0372
Total (mm^2)	0.808			

Table 3. Estimated footprint for each component.

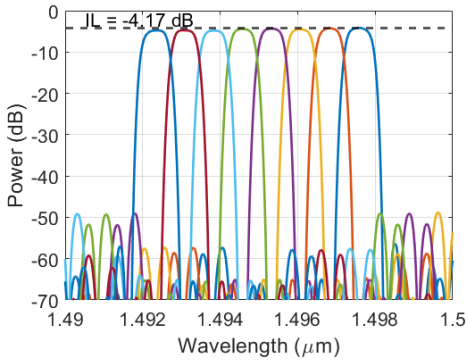

(a)

Component	Through port	Drop port
Crossing (dB)	0.04	–
MZI (dB)	0.35	–
CDC (dB)	0.18	0.60

(b)

Fig. 7. (a) Broadband measured spectrum after propagation through the 1×3 WSS (S-band). (b) Individual insertion losses for each component.

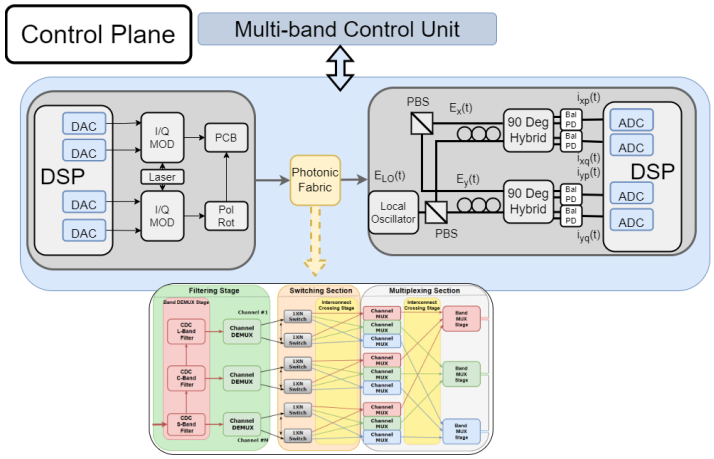

Fig. 8. Control abstraction of the optical switch for the proposed SDN-controlled transmission system.

Having characterized the spectral response of the main components and their losses for the envisioned S+C+L WSS, the next section will present an application of the Software-Defined Networking (SDN) paradigm to abstract the physical layer properties of this device.

3. Software-defined network application to the WDM transport layer

SDN is based on a network controller that manages transmission and switching elements to optimize performance, that is, maximize transmission capacity (Fig. 8). Generally, in the SDN framework, an open interface for the control and a model for its transmission impairments are required for each transmission element. For physical channels, the SDN implementation requires the capability to summarize the QoT of physical layer links using a proper metric, so we need the availability of a QoT-estimator (QoT-E). The introduction of optical fiber transmission systems of coherent TRXs based on dual-polarization multilevel modulation formats simplified the application of SDN to WDM optical transport. Exploiting such transmission technology empowers modeling a transparent LP within the photonic transmission system as an Additive White Gaussian Noise (AWGN) channel whose QoT is fully characterized by the LP OSNR.

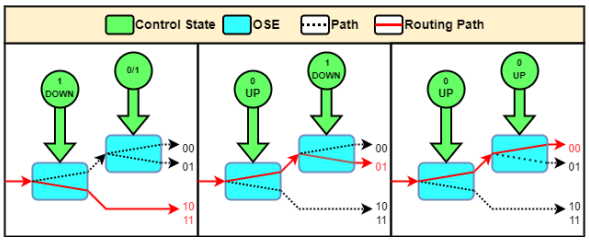

Fig. 9. Switching sub-network configurations.

Such propagation modeling of transparent LP also enables simple TRXs modeling that can be characterized in the back-to-back configuration to define the requested minimum OSNR for LP feasibility. This approach enables the virtualization of the optical transport by using a QoT-E that computes the LP OSNR and compares it to the minimum OSNR requested by the TRX. Using coherent TRXs, a transparent LP can be dynamically set from the source to destination within the photonic transmission system by correctly setting the optical switches. To properly deploy LPs, the network controller must evaluate QoT degradation effectively across the entire path of the selected LP. Models are needed to evaluate the QoT degradation of each crossed transmission and switching element. In addition to QoT degradation, the SDN controller also needs algorithms to define the optimal operating point that minimizes QoT degradation.

In this direction, the following section focuses on the control and QoT degradation model for the proposed WSS architecture. The control section is manipulated through two distinct parts: switching control and fine-frequency thermal tuning of the filtering elements. At the same time, a deterministic technique is used to evaluate QoT and is tested on a system that operates on 400ZR standards.

3.1. Control and filter alignment

In order to implement the SDN paradigm, the network operator must be able to deploy and manage the required LPs. As described in Section 2.2, the target routing of each channel is achieved by driving the underlying switching sub-networks. The controller must have a virtualized model of the WSS device to evaluate the required control signals. For the proposed implementation scenario, with three possible output fibers, each switching sub-network is composed of two OSE, thus allowing four separate control configurations. The possible routing states of the networks are depicted in Fig. 9, together with the logical table describing the achievable states. Due to the limited number of output fibers, the switching circuit is quite elementary, but highlights the general model for routing evaluation. The topology of this structure can be modeled as a binary tree, which represents a well-known class of data structures. The control states of the OSE can be obtained directly from the target output fiber.

By representing the output fibers in binary, each bit represents the propagation direction at each encountered node, under the convention $1 \Rightarrow$ DOWN and $0 \Rightarrow$ UP. Therefore, the total number of output fibers N and the label of the target output port are enough to evaluate the control states for the given request using a fast and low-cost deterministic algorithm. The proposed path-finding algorithm is rigorously defined for $N = 2^x$, $x \in \mathbb{N}$, although it can be easily generalized: in the configuration table for the 1×3 network, both "10" and "11" are considered valid routing tags for output fiber 3, as the signal encounters only a single OSE, thus not requiring any control status for the last stage.

In addition to routing control of the OSE, the proposed device grants an additional degree of freedom with respect to fixed-frequency WSS structures. Although each CDC add/drop element is tailored for a precise central operating frequency and bandwidth, the working frequencies of these elements can be fine-tuned through thermal control to allow calibration and compensation of manufacturing uncertainty, as well as different transmission scenarios with respect to the one

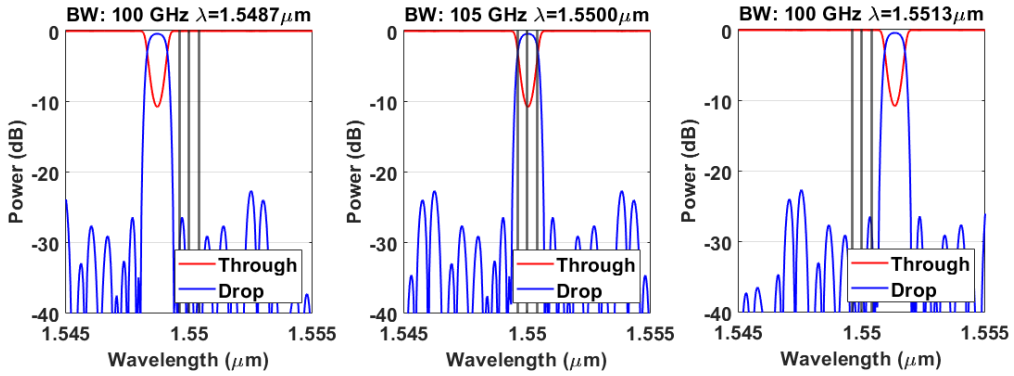

Fig. 10. Channel tuning for a considered temperature shift $\Delta T = [-30, 0, 30]$°C. Central channel wavelength and 3dB bandwidth are highlighted by the gray lines.

assumed in the original design. Although thermal control applied to MZI structures represents a binary control of the switching path, thermo-optical effects can be used to align the central response of the CDC to the target frequency and some control of the channel bandwidth [24]. In this analysis, the band-flexible capabilities of these devices are not considered; as such, the main focus rests on channel alignment.

As shown in Fig. 10 this effect cannot be exploited to operate the device in a distant frequency band, although it can be used to align the filtering elements with different WDM combs, which is compatible with the tunability of other PIC implementations, such as the ones using Array Waveguide Gratings (AWG) [25]. However, thermal tuning represents an expensive solution from a power consumption point of view; as such, filter elements should also be manufactured and designed following methods that minimize the effect of fabrication tolerances [26].

3.2. QoT evaluation

The WSS penalty has been characterized by simulating the device in a coherent transmission scenario in the OptSim© PIC design and simulation environment. Transmission parameters have been chosen to conform to the 400ZR standard [27], using dual-polarization 16QAM modulation and a symbol rate R_S=60 GBaud, with a channel spacing of FSR=100 GHz. The WDM combs of each of the bands are placed in their respective centers, with the channel occupancy highlighted in the response of the components shown in the previous sections. This provides a reasonable and realistic benchmark to evaluate the performance of the proposed device.

Transmission impairments have been characterized as Optical Signal-to-Noise Ratio penalty (ΔOSNR), bench-marking link performances to the unfiltered case in back-to-back conditions. This metric was extracted by simulating the Bit-Error Rate (BER) as a function of the receiver-added noise. It has been evaluated for all possible configurations of the device, using a reference bit-error-rate threshold $\mathrm{BER_{th}} = 10^{-3}$. Given the relatively flat response of all internal components of the proposed WSS and the previously discussed MUX/DEMUX symmetry, the path-dependent penalty is primarily related to the number of waveguide crossings encountered. Due to the device interconnect symmetry, the same distribution is seen for links targeting the first and last output fibers. On the contrary, the central output fiber shows the same number of crossings encountered, independently of the channel origin. This behavior is evident when observing the crossing topology described in the previous section, see Fig. 6: every channel Ch_i , $i \in [1:8]$ of each band targeting the central fiber output needs to cross all the links of the previous channels ($\mathrm{Ch}_{1:i-1}$) targeting the third output, and also all the ones of the following channels ($\mathrm{Ch}_{i+1:8}$) targeting the first output fiber, which always balance to the same number of encountered elements.

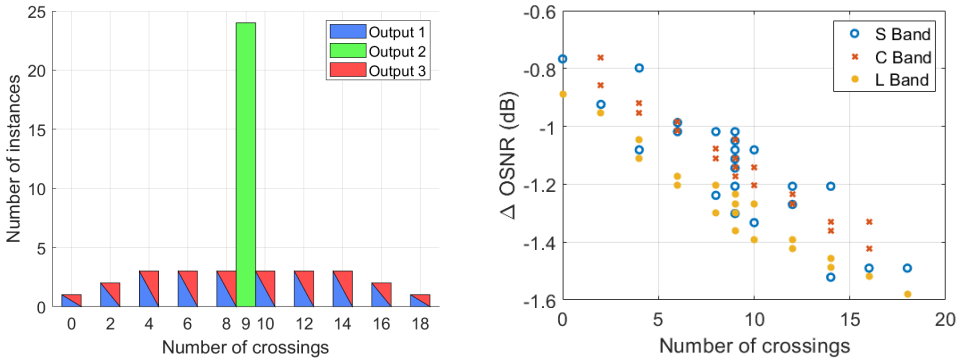

Fig. 11. Architecture penalty model, highlighting the encountered crossing distribution (a) and the calculated transmission penalty ΔOSNR (b).

This allows the characterization of the device configuration in terms of the number of encountered crossings, thanks to the intrinsic bijective routing nature of the device. In traditional multistage switching architectures, multiple routing paths may exist between the same input-output pair, while in the proposed topology, only one link exists for each possible input-output combination.

The observed OSNR penalties are shown in Fig. 11 as a function of the number of crossings, highlighting consistent performances with respect to alternative solutions present in the literature [28]. The relationship clearly shows a linear dependence, confirming the critical role of the waveguide interconnects in determining the configuration penalty with respect to the flat degradation introduced by the filtering and switching elements, which can be observed in the zero-crossing case. This behavior of the model is not surprising because of the responses of each individual element, which introduces flat frequency-independent losses in the bandwidth of interest. The important concept showcased by these results is the possibility of reducing the complexity of device characterization by analyzing the unique topological structure rather than all configurations of the device. Taking into account the proposed case study, with 24 independent channels and 3 output fibers, a complete study of control states and penalties would require the analysis of 3^{24} ($\approx 3 \times 10^{11}$) cases which are clearly unfeasible. By exploiting the known topology as well as the virtualized model of the device, the required number of needed simulations is drastically reduced, with only 72 cases that need to be tested to get the penalty of all channels, considering the independent routing of each of them, as well as the limited component crosstalk. These compact data sets can be used to characterize transmission impairment for each channel in any possible switching configuration, allowing the SDN operator to quickly estimate and predict the expected ΔOSNR penalties. Furthermore, the linear relationship between the crossing number and penalty can be used to quickly estimate the penalty margin for any given channel for scaled devices: given the modularity of the architecture, increasing channels and ports number lead to a unique crossing topology and distribution, which can be quickly assessed.

In the proposed simulation, each component behaves exactly as designed, with no significant differences between multiple instances. In reality, due to manufacturing uncertainty, the penalty introduced by nominally identical elements could be different, which could drastically alter the linear relationship showcased in the simulations. Even in this scenario, though the proposed control and evaluation scheme is effective, since the required data set using a look-up table strategy grows identically to the size of the device, with a linear relationship $O(NM)$, which does not pose any scalability issue from the controller point of view with respect to more traditional multi-stage switching devices [29, 30].

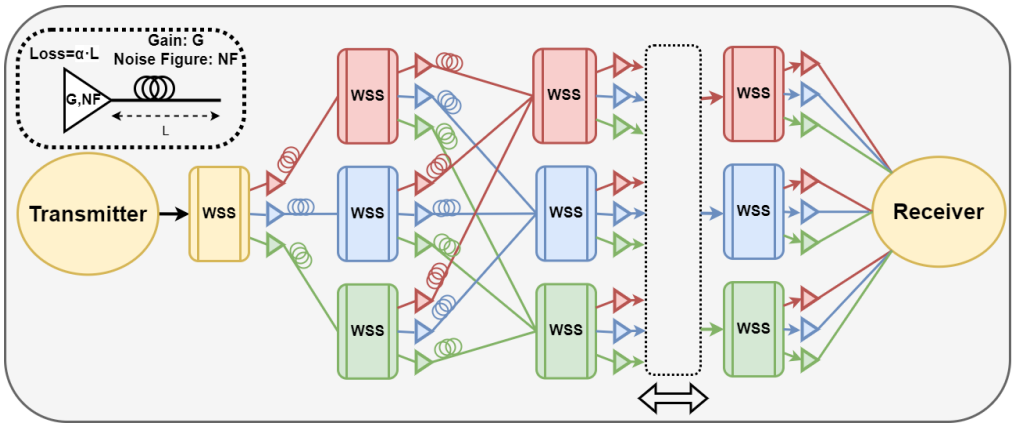

Fig. 12. Proposed arbitrary-size WSS cascade used as testbed for the characterization of the system OSNR.

	S-band	C-band	L-band
Amplifier type	TDFA	EDFA	EDFA
Loss α (dB/km)	0.20	0.19	0.18
Gain G (dB)	15.0	14.3	13.5
Noise Figure NF (dB)	6.50	4.25	4.68

Table 4. OLS parameters used in the proposed network simulation.

4. Networking scenario case-study

After analyzing the proposed WSS device from the physical level (Section I) and its behavior from a transmission-level point of view (Section II), we offer a simple case study to contextualize the element in a networking scenario. In this study, we can account for the cascade of multiple instances of the proposed WSS device. The simulation testbed is shown in Fig. 12. To simplify the analysis, the system is considered a point-to-point network with an arbitrary number of WSS stages N_{stages}, allowing the characterization of the WSS performance for a variable number of hops. The system presents a single start and end point, with the receiver side collecting the data for all possible paths that each channel can traverse. At each stage, any given channel can be routed to three different target WSS devices of the following stages, allowing a total number of configurations of $N_{\text{config}} = 3^{N_{\text{stages}}}$ for each individual channel. Optical Line Systems (OLSs) connecting each stage are characterized for each of the S+C+L bands with the same fiber but different amplifier types based on the band of operation. The commercially available Erbium-Doped Fiber Amplifiers (EDFAs) are considered for channels in the C- and L- bands. In the S-band, the amplifier with a benchtop Thulium-Doped Fiber Amplifier (TDFA) with the characteristics reported in [31] is considered.

The proposed simulation scenario only considers the standard fiber losses and the linear part of the impairments, i.e., the Amplified Spontaneous Emission (ASE) noise. Parameters for the OLSs in each operating band are reported in Table 4 [32]. The cumulative LP OSNR at each given stage can be evaluated as:

$$\text{OSNR} = \frac{1}{\sum_{i=1}^{N_{\text{stages}}} \frac{1}{\text{OSNR}_i}} \quad \text{with} \quad \text{OSNR}_i = \frac{P_{\text{Rx}}}{P_{\text{ASE}_i}} \tag{1}$$

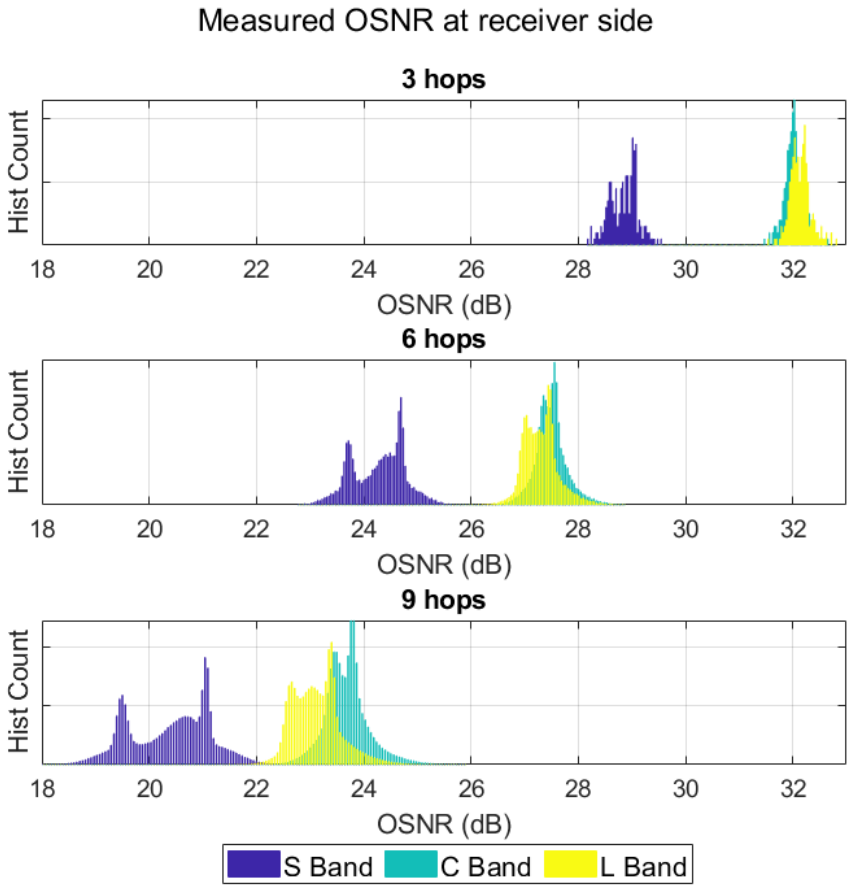

Fig. 13. Calculated OSNR at the receiver for different number of network hops. The performances of the three considered bands are highlighted separately.

where P_{Rx} is the power of the channel at the receiver, P_{ASE} is the power of the accumulated ASE noise in a reference noise bandwidth of 12.5 GHz, for the considered channel. The Noise Figure (NF) and Gain (G) are selected based on the band of interest, as shown already in Table 4 (for more details see [32]), considering a reference span length of $L = 75$ km. The proposed simulation has been conducted assuming span (and OLS) transparency; as such, the power loss introduced by the fiber lines is fully compensated by the amplifier so that at the ingress of each stage $P_{\mathrm{in}} = P_0 = 0$ dBm. The OSNR is calculated at the receiver. The penalty introduced by the WSS devices has been evaluated using data from the transmission-level simulation, introducing the cascaded penalty obtained for the specific channel under the requested routing in the network. The simulation was carried out for every possible channel path from the source node to the destination node.

The simulated OSNR distribution in three operating bands on the receiver side is shown in Fig. 13 for three different network scenarios, corresponding to a 3, 6 and 9 stage WSS cascade, respectively. The overall QoT in Fig. 13 exhibits a strong frequency dependency, although this is mainly due to the different OLS parameters used in the S-, C-, and L-bands. The WSS-added penalty (Fig. 14a) after 3 hops clearly shows a slight asymmetry in the penalty distribution of the three bands, albeit confined in the same region, with misaligned distribution peaks. Similar behavior is also demonstrated for larger network scenarios with 6 and 9 network hops, as depicted

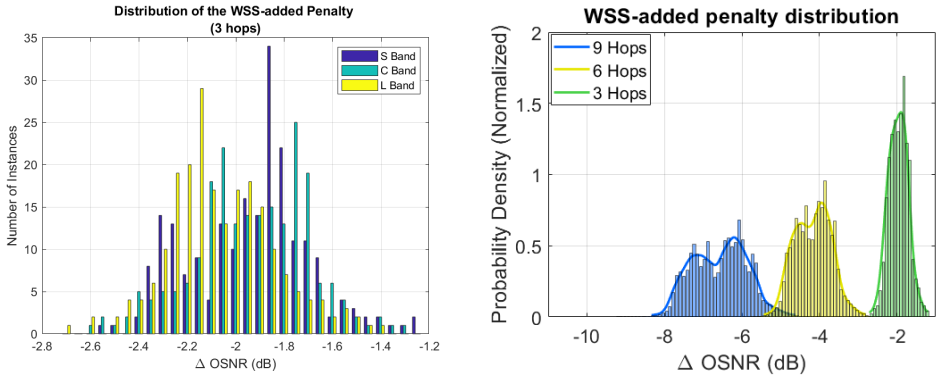

(a) (b)

Fig. 14. OSNR Penalty distribution for different numbers of network hops. (a) Highlight of the distribution of the three bands after three hops; (b) global distribution for increasing network size.

in Fig. 14b. Aside from the increase in the OSNR penalty and the broadening of the range, which is expected, the penalty distribution begins to exhibit bimodal behavior. The bimodality primarily emerges due to the previously highlighted band asymmetry, but even after 9 networks hops the effect is still reasonably weak, especially compared to the OLS effects, which are the main elements responsible for the band separation. Overall, the resulting behavior of this network case study validates the assumption of the control data set proposed in Section 3: the slight asymmetry between QoT in the three transmission bands is limited even when multiple instances are cascaded in the same network, as such the proposed average value control strategy could yield faster yet practical results. Taking into account the 72-data-point approach, which takes into account the difference between the penalty distributions in each band and each routing case, the full characterization of the device highlights the applicability of the architecture to the multi-band scenario.

The device has been shown to maintain its low-loss, low-penalty behavior, and flat multi-band performance even in a multi-stage cascade.

5. Conclusion

We proposed a novel integrated photonic multi-band WSS, which can support a broad range of the optical spectrum, including the S+C+L bands, which can act as a fundamental building block in modern optical networking. The design of such a device was presented in detail, discussing both the first filtering section and the following routing section. A software abstraction of the designed WSS was obtained by its full characterization using a deterministic model, which can potentially estimate the routing controls and the expected QoT degradation of the proposed multi-band WSS architecture. In addition to this, a network case study was also performed to evaluate the performance of the proposed WSS in a single and cascade operation. The results demonstrate that the proposed device offers low-loss and frequency-flat behavior for the considered bands of operation in a single or cascade implementation. The fully integrated architecture designed can achieve its operation as envisioned, resulting in compatible performances with respect to alternative solutions while offering increased modularity and high customizability for multiple dense WDM applications.

Funding. This work was supported by the Synopsys within the activities of a research MSA with Politecnico di Torino and by the European Union's Horizon 2020 research and innovation programme under the Marie Skłodowska-Curie grant agreement 814276.

Disclosures. The authors declare no conflicts of interest.

Data Availability Statement. Data underlying the results presented in this article are not publicly available at this time, but may be obtained from the authors upon reasonable request.

References

1. A. Napoli, M. Bohn, D. Rafique, A. Stavdas, N. Sambo, L. Poti, M. Nolle, J. K. Fischer, E. Riccardi, A. Pagano, A. Di Giglio, M. S. Moreolo, J. M. Fabrega, E. Hugues-Salas, G. Zervas, D. Simeonidou, P. Layec, A. D'Errico, T. Rahman, and J. P. F.-P. Gimenez, "Next generation elastic optical networks: The vision of the european research project idealist," IEEE communications magazine **53**, 152–162 (2015).
2. Cisco, "Cisco annual internet report (2018–2023) white paper," (2020).
3. J. Pedro, N. Costa, and S. Pato, "Optical transport network design beyond 100 GBaud," JOCN **12**, A123–A134 (2020).
4. A. Ferrari, A. Napoli, J. K. Fischer, N. Costa, A. D'Amico, J. Pedro, W. Forysiak, E. Pincemin, A. Lord, A. Stavdas, J. P. F.-P. Gimenez, G. Roelkens, N. Calabretta, S. Abrate, B. Sommerkorn-Krombholz, and V. Curri, "Assessment on the achievable throughput of multi-band ITU-T G.652.D fiber transmission systems," J. Light. Technol. **38**, 4279–4291 (2020).
5. V. Curri, "Multiband optical transport: a cost-effective and seamless increase of network capacity," in *OSA Advanced Photonics Congress 2021,* (Optical Society of America, 2021), p. NeTu2C.3.
6. T. A. Strasser and J. L. Wagener, "Wavelength-selective switches for ROADM applications," IEEE J. Sel. Top. Quantum Electron. **16**, 1150–1157 (2010).
7. R. Kraemer, F. Nakamura, M. v. d. Hout, S. van der Heide, C. Okonkwo, H. Tsuda, A. Napoli, and N. Calabretta, "Multi-band photonic integrated wavelength selective switch," J. Light. Technol. **39**, 6023–6032 (2021).
8. V. Curri, "Software-defined WDM optical transport in disaggregated open optical networks," in *22nd International Conference on Transparent Optical Networks (ICTON),* (2020).
9. I. Khan, L. Tunesi, M. U. Masood, E. Ghillino, P. Bardella, A. Carena, and V. Curri, "Automatic management of N×N photonic switch powered by machine learning in software-defined optical transport," IEEE Open J. Commun. Soc. **2**, 1358–1365 (2021).
10. I. Khan, L. Tunesi, M. Chalony, E. Ghillino, M. U. Masood, J. Patel, P. Bardella, A. Carena, and V. Curri, "Machine-learning-aided abstraction of photonic integrated circuits in software-defined optical transport," in *Next-Generation Optical Communication: Components, Sub-Systems, and Systems X,* vol. 11713 (SPIE, 2021).
11. J.-P. Weber, "Spectral characteristics of coupled-waveguide bragg-reflection tunable optical filter," IEE Proc. J (Optoelectronics) **140**, 275–284(9) (1993).
12. M. Hammood, A. Mistry, H. Yun, M. Ma, S. Lin, L. Chrostowski, and N. A. F. Jaeger, "Broadband, silicon photonic, optical add–drop filters with 3 db bandwidths up to 11 thz," Opt. Lett. **46**, 2738–2741 (2021).
13. W. Shi, M. Greenberg, X. Wang, Y. Wang, C. Lin, N. A. F. Jaeger, and L. Chrostowski, "Single-band add-drop filters using anti-reflection, contra-directional couplers," in *The 9th International Conference on Group IV Photonics (GFP),* (2012), pp. 21–23.
14. H. Qiu, J. Jiang, P. Yu, D. Mu, J. Yang, X. Jiang, H. Yu, R. Cheng, and L. Chrostowski, "Narrow-band add-drop filter based on phase-modulated grating-assisted contra-directional couplers," J. Light. Technol. **36**, 3760–3764 (2018).
15. X. Tu, C. Song, T. Huang, Z. Chen, and H. Fu, "State of the art and perspectives on silicon photonic switches," Micromachines **10** (2019).
16. N. Dupuis, A. V. Rylyakov, C. L. Schow, D. M. Kuchta, C. W. Baks, J. S. Orcutt, D. M. Gill, W. M. J. Green, and B. G. Lee, "Ultralow crosstalk nanosecond-scale nested 2 × 2 Mach–Zehnder silicon photonic switch," Opt. Lett. **41**, 3002–3005 (2016).
17. Z. Lu, D. Celo, H. Mehrvar, E. Bernier, and L. Chrostowski, "High-performance silicon photonic tri-state switch based on balanced nested mach-zehnder interferometer," Sci. Reports **7**, 12244 (2017).
18. S. Liu, J. Feng, Y. Tian, H. Zhao, L. Jin, B. Ouyang, J. Zhu, and J. Guo, "Thermo-optic phase shifters based on silicon-on-insulator platform: state-of-the-art and a review," Front. Optoelectron. **15**, 9 (2022).
19. D. Yi, W. Zhou, Y. Zhang, and H. K. Tsang, "Inverse design of multi-band and wideband waveguide crossings," Opt. Lett. **46**, 884–887 (2021).
20. Z. Yu, A. Feng, X. Xi, and X. Sun, "Inverse-designed low-loss and wideband polarization-insensitive silicon waveguide crossing," Opt. Lett. **44**, 77–80 (2019).
21. S. Wu, X. Mu, L. Cheng, S. Mao, and H. Fu, "State-of-the-art and perspectives on silicon waveguide crossings: A review," Micromachines **11** (2020).
22. S. Zhao, L. Lu, L. Zhou, D. Li, Z. Guo, and J. Chen, "16×16 silicon Mach–Zehnder interferometer switch actuated with waveguide microheaters," Photon. Res. **4**, 202–207 (2016).
23. T. Yoshida, H. Asakura, H. Tsuda, T. Mizuno, and H. Takahashi, "Switching characteristics of a 100-GHz-spacing integrated 40-λ 1 × 4 wavelength selective switch," IEEE Photonics Technol. Lett. **26**, 451–453 (2014).
24. J. Cauchon, J. St-Yves, and W. Shi, "Thermally chirped contra-directional couplers for residueless, bandwidth-tunable bragg filters with fabrication error compensation," Opt. Lett. **46**, 532–535 (2021).
25. Y. Yang, X. Hu, J. Song, Q. Fang, M. Yu, X. Tu, G.-Q. Lo, and Rusli, "Thermo-optically tunable silicon AWG with above 600 GHz channel tunability," IEEE Photonics Technol. Lett. **27**, 2351–2354 (2015).
26. M. Nikdast, G. Nicolescu, J. Trajkovic, and O. Liboiron-Ladouceur, "Modeling fabrication non-uniformity in chip-scale silicon photonic interconnects," in *2016 Design, Automation & Test in Europe Conference & Exhibition*

(DATE), (2016), pp. 115–120.
27. Implementation agreement for a 400ZR coherent optical interface, https://www.oiforum.com/technical-work/hot-topics/400zr-2/.
28. R. Kraemer, F. Nakamura, M. v. d. Hout, S. van der Heide, C. Okonkwo, H. Tsuda, A. Napoli, and N. Calabretta, "Multi-band photonic integrated wavelength selective switch," J. Light. Technol. **39**, 6023–6032 (2021).
29. I. Khan, L. Tunesi, M. U. Masood, E. Ghillino, P. Bardella, A. Carena, and V. Curri, "Machine learning assisted model of qot penalties for photonics switching systems," in *Photonics in Switching and Computing 2021,* (Optical Society of America, 2021), p. M2A.3.
30. I. Khan, L. Tunesi, M. U. Masood, E. Ghillino, P. Bardella, A. Carena, and V. Curri, "Performance evaluation of data-driven techniques for softwarized and agnostic management of N×N photonic switch," Opt. Continuum **1** (2022).
31. Fiberlabs, https://www.fiberlabs.com/.
32. B. Correia, R. Sadeghi, E. Virgillito, A. Napoli, N. Costa, J. Pedro, and V. Curri, "Power control strategies and network performance assessment for C+L+S multiband optical transport," J. Opt. Commun. Netw. **13**, 147–157 (2021).